Large uncertainty in volcanic aerosol radiative forcing derived from ice cores

Lauren Marshall[1,2,*], Anja Schmidt[2,3], Jill S. Johnson[1], Graham W. Mann[1,4], Lindsay Lee[1] and Ken S. Carslaw[1]

[1]School of Earth and Environment, University of Leeds, Leeds, UK

[2]Department of Chemistry, University of Cambridge, Cambridge, UK

[3]Department of Geography, University of Cambridge, Cambridge, UK

[4]National Centre for Atmospheric Science, University of Leeds, Leeds, UK

[*]Corresponding author: Lauren Marshall (lrm49@cam.ac.uk)

This is a non-peer reviewed preprint submitted to EarthArXiv

Submitted to Nature Communications

Abstract

Reconstructions of volcanic aerosol radiative forcing are required to understand past climate variability. Currently, reconstructions of pre-20th century volcanic forcing are derived from sulfate concentrations measured in polar ice cores, predominantly using a relationship between average ice sheet sulfate deposition and stratospheric sulfate aerosol based on a single explosive eruption - the 1991 eruption of Mt. Pinatubo. Here we derive volcanic radiative forcing from ice-core-records using a perturbed parameter ensemble of aerosol-climate model simulations of explosive eruptions, which enables the uncertainty to be estimated. We find that a very wide range of eruptions with different sulfur dioxide emissions, eruption latitudes, emission altitudes and in different seasons produce ice-sheet sulfate deposition consistent with ice-core-derived values for eruptions during the last 2500 years. Consequently, we find a large uncertainty in the volcanic forcing, suggesting uncertainties on the global mean temperature response of more than 1°C for several past explosive eruptions, which has not been previously accounted for.

Introduction

Explosive volcanic eruptions that inject large amounts of sulfur dioxide (SO_2) into the stratosphere are major drivers of natural climate variability on multi-annual to decadal timescales[1]. The SO_2 is converted to sulfate aerosol, which causes a radiative perturbation, or forcing, by scattering incoming solar radiation, and leads to surface and tropospheric cooling. Reconstructions of volcanic aerosol radiative forcing are therefore required to understand and attribute climate variability on millennial timescales[2-4] and are used as input to climate model simulations[5,6]. Correct reconstructions of all climate forcing agents are vital to understand and evaluate past temperature changes on global and regional scales, to assess ocean heat uptake, which is critical for estimating future sea-level rise, and ultimately to compare natural and anthropogenic drivers of climate variability.

Reconstructions of volcanic radiative forcing are uncertain because of the lack of in-situ and remote-sensing measurements for eruptions before the 1963 eruption of Mt. Agung. When available in the modern era, SO_2 emissions and stratospheric aerosol optical depth (sAOD) are derived from satellite retrievals (since ~1979)[7] and ground-based optical measurements (since ~1800s)[8-10]. When direct measurements are not available, volcanic forcing datasets are constructed based on sulfate concentration anomalies measured in ice cores. Alternatively, the injected mass of sulfur can be estimated from petrological and geochemical studies of eruption deposits[11-15].

Sulfate measured in ice cores provides a record of volcanism with high temporal resolution over thousands of years[4,16]. However, several assumptions must be made to translate the record of sulfate anomalies into a record of radiative forcing. Established methods include using transfer functions to estimate hemispheric stratospheric sulfate aerosol burdens (i.e. the total mass of volcanic sulfate aerosol in the stratosphere of each hemisphere)[4,17,18] or sAOD[19] from estimates of the average amount of sulfate deposited on each ice sheet. Transfer functions are derived from the ice-sheet deposition averages and observed stratospheric sulfate burden or sAOD following the 1991 eruption of Mt. Pinatubo, from estimates of radioactive material in the stratosphere and measured in ice cores following nuclear weapons testing in the 1950s and 1960s[20] or from climate model simulations[21].

Several factors can affect the relationship between ice-sheet sulfate deposition and stratospheric sulfate burdens and sAOD, therefore it is unlikely that these transfer functions are entirely applicable to eruptions other than 1991 Mt. Pinatubo. For example, several studies have shown that polar sulfate deposition is modulated by the season[17,22,23], atmospheric variability[22,24] and the magnitude of the injection, which can alter atmospheric circulation[22]. In addition, the radiative forcing efficiency per unit mass of emitted sulfur falls with increasing SO_2 emission size due to creation of larger sulfate aerosol particles[25,26]. Further uncertainties are associated with the conversion of estimated sulfate aerosol burdens into sAOD and radiative forcing. For the reconstruction of Gao et al. (2008)[17], a linear scaling is applied between the sulfate aerosol burden and sAOD [(27)]. Other reconstructions scale ice-sheet-sulfate-deposition to sAOD based on this relationship after 1991 Mt. Pinatubo but attempt to account for changes to particle sizes for eruptions with larger SO_2 emissions by applying an idealized 2/3 power scaling[18,19]. sAOD can then be converted to radiative forcing using further conversion factors based on climate model simulations of the 1991 eruption of Mt. Pinatubo[28]. However, the relationship between sAOD and radiative forcing is uncertain as it is dependent on the aerosol particle size distribution[29], the latitude and season of an eruption[30], aerosol-cloud interactions[31-33] and model configuration[1,28,34].

Simulations of the last millennium as part of the Paleoclimate Modelling Intercomparison Project phase 4 (PMIP4) will use the prescribed sAOD forcing timeseries 'EVA(2k)' derived by Toohey and Sigl (2017)[18], where the radiative forcing is calculated internally by each model. The spatial and temporal evolution of the prescribed sAOD is based on a simple parameterized transport model, the Easy Volcanic Aerosol (EVA) forcing generator[35], which uses stratospheric SO_2 emissions from the eVolv2k reconstruction[18]. The EVA forcing generator is calibrated against the measured evolution of stratospheric aerosol following the 1991 Mt. Pinatubo eruption and does not account for many microphysical, chemical and dynamical processes that occur following a volcanic eruption. Because many eruptions identified in ice-core sulfate records are unattributed, the eruption season and latitude must be estimated or arbitrarily assigned, which introduces further uncertainty because these factors affect the formation and transport of stratospheric sulfate aerosol and its deposition[17,22,36]. Eruptions are assumed to be tropical if simultaneous sulfate signals occur in both Antarctica and Greenland (bipolar deposition signals) and are assigned to January if the season is unknown.

The difficulty with any reconstruction of radiative forcing is that it does not scale directly with the ice-sheet-deposited sulfate. The magnitude of the forcing (integrated over time) depends on the global spread of the volcanic aerosol in the stratosphere, its lifetime, and the microphysical properties of the aerosol (size, mass and number of the aerosol particles). All of these depend on the emission strength, the altitude and latitude of emission and the eruption season, so-called 'eruption source parameters' [37]. Consequently, for any observed ice core volcanic sulfate deposition there is potentially a very wide range of 'eruption-realisations' (i.e. eruptions with different combinations of SO_2 emission, eruption latitude, emission altitude and eruption season) with a wide range of associated forcings.

Some attempts have been made to estimate the uncertainty in SO_2 emissions derived from ice-core sulfate composites by considering uncertainties in the ice-core composites themselves and in the transfer functions[18] but the possible range in radiative forcing has not yet been properly quantified.

Previous sensitivity studies investigating the relationships between eruption source parameters and sulfate deposition have also been based on specific case-studies[23] or at single latitudes[22].

Here, we investigate and quantify comprehensively the uncertainty in volcanic aerosol radiative forcing derived from ice-core sulfate records. Using a state-of-the-art aerosol-climate model, we simulate a wide range of large-magnitude explosive eruptions and use the results to build statistical emulators that describe how sulfate deposition and time-integrated radiative forcing vary with eruption magnitude, eruption latitude, injection height and eruption season[37] (see Methods). The emulators enable us to predict the sulfate deposition and radiative forcing for thousands of eruptions that we did not simulate directly. We examine the combinations of eruption source parameters that could lead to measured ice-sheet sulfate deposition for ten of the largest deposition signals recorded in the last 2500 years and estimate the associated range in radiative forcings. Consequently, we calculate the radiative forcing of eruptions from ice-core sulfate records independently of transfer functions and conversion factors, allowing us to assess their applicability in deriving volcanic forcing reconstructions.

Results

Simulated ice-sheet sulfate deposition

We simulated 82 explosive volcanic eruptions with the UM-UKCA model, each with a different SO_2 emission (between 10 and 100 Tg of SO_2), eruption latitude (between 80°S and 80°N) and injection height (between 16.5 and 26.5 km with a 3-km-deep plume), and for an eruption occurring in January and July (see Methods). Simulated ice-sheet volcanic sulfate deposition is greater for eruptions with the largest SO_2 emissions that are also close to each ice sheet (Fig. 1). Because the deposition is dependent on both the SO_2 emission and the eruption latitude, there are eruptions that are close to the ice sheets but have low deposition because the SO_2 emission was low, and eruptions with high SO_2 emissions but low deposition because they are far away from the ice sheet. We do not find an obvious relationship between the injection height of the SO_2 emissions and the magnitude of the ice-sheet sulfate deposition.

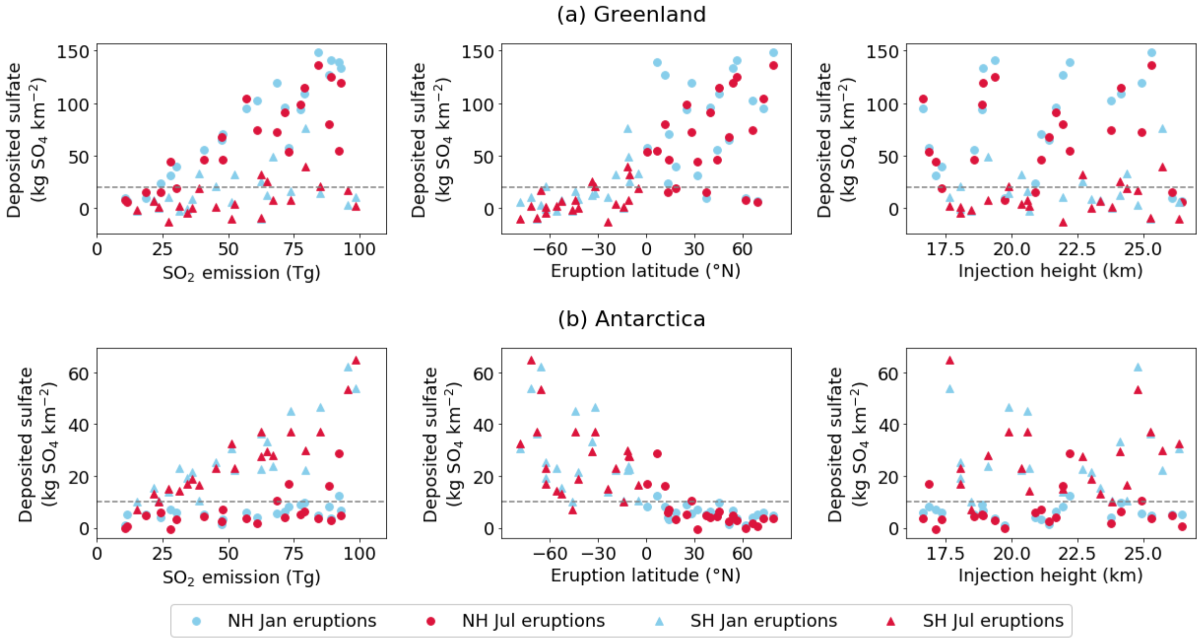

Fig. 1 Time-integrated volcanic sulfate deposited on (a) Greenland and (b) Antarctica in each simulation versus the value of SO_2 emission (left), eruption latitude (middle) and injection height (right) in that simulation. Volcanic deposited sulfate is calculated by subtracting the climatological deposited sulfate from the deposited sulfate in each simulation (see Methods). Deposition from the January eruptions are shown in blue and in red for the July eruptions. Northern hemisphere (NH) eruptions are shown by the circle markers; southern hemisphere (SH) eruptions are shown by the triangular markers. There are different scales on the y axes between (a) and (b). Injection height marks the middle of the 3-km deep plume (see Methods). The horizontal grey dashed lines mark approximate thresholds above which a volcanic signal becomes clear (20 kg km^{-2} on Greenland and 10 kg km^{-2} on Antarctica; see text).

On average, the deposition of sulfate (SO_4) on Greenland is higher than on Antarctica, with a maximum of 148 kg km^{-2} deposited for an eruption at 79°N occurring in January, with a SO_2 emission of 84 Tg. The maximum simulated Antarctica deposition of 65 kg km^{-2} occurs for a July eruption at 72°S with a SO_2 emission of 98 Tg. Lower deposition on Antarctica compared to Greenland was also found in a previous study of tropical eruptions[22], most likely due to stronger meridional transport in the Northern Hemisphere (NH) and increased deposition because the NH is relatively more dynamically active than the Southern Hemisphere (SH). In the SH the stronger polar vortex will inhibit more of the poleward aerosol transport. Deposition on the ice sheets will also vary with SO_2 emission magnitude given an increase in sedimentation as particles grow larger such that they may be deposited before reaching the ice sheets, and stronger polar vortices arising from aerosol-induced stratospheric heating[22,38].

Deposition on Greenland is greater for tropical eruptions occurring in January (blue circles in Fig. 1a) because more sulfate aerosol is transported to the NH via the Brewer Dobson Circulation (BDC), which is stronger in the winter hemisphere. Similarly, both total SH deposition (Supplementary Fig. 1) and deposition on Antarctica from tropical eruptions is greater if they occur in July (red circles in Fig. 1b) following the seasonal cycle of the BDC. For eruptions at latitudes greater than ~30°N/S the total hemispheric deposition is similar between the seasons (Supplementary Fig. 1), however ice-sheet deposition varies between seasons, but is not consistently larger in either one. Differences in the ice-sheet deposition following eruptions in different seasons for mid-to-high latitude eruptions could be dependent on the SO_2 emission magnitude, injection height, and seasonal variations in stratosphere-troposphere exchange and sulfate aerosol deposition rates in the mid-latitude storm tracks[39]. Seasonal differences may also arise due to internal variability.

There is also considerable scatter in the deposition values around zero for eruptions located at high latitudes in the opposite hemisphere to the ice sheet, which has implications for the detection and quantification of volcanic events. We find that the ice-sheet deposition time series are very noisy because of internal variability, which can obscure or enhance the deposition (Supplementary Fig. 2). This is because the difference between the ice sheet sulfate deposition in the volcanically perturbed simulations and in the control simulation (see Methods) is affected by volcanic sulfate deposition, as well as by variations in the background tropospheric sulfate aerosol deposition caused by the effect of the eruption on stratospheric and tropospheric dynamics (i.e. the control and perturbed runs effectively behave like two meteorological ensemble members). Consequently, the amount of background tropospheric-originating sulfate aerosol can be very different in each perturbed simulation compared to the control climatology. Time-integrated deposition anomalies can even be negative because the climatological deposition is higher than in the perturbed simulation, which represents just one possible realisation of reality (an example is shown in Supplementary Fig. 2). Our analysis of a wide range of simulated eruptions highlights the inherent difficulty in detecting and quantifying volcanic deposition anomalies in ice cores. The volcanic sulfate deposition signal on Greenland becomes clear only for anomalies that exceed ~20 kg km^{-2} and for Antarctica when anomalies exceed ~10 kg km^{-2} (Fig. 1; grey lines).

Ice-sheet sulfate deposition predicted for thousands of eruptions

By replacing the UM-UKCA model with statistical emulators that describe how the ice-sheet deposition varies with SO_2 emission, eruption latitude and injection height, we can predict the sulfate deposition for any eruption that we did not directly simulate (see Methods). The emulators, which are built for January and July eruptions separately, enable us to examine the relationship between ice-sheet sulfate deposition and the eruption source parameters in unprecedented detail because the emulated predictions for all possible eruptions in our three-dimensional parameter space describe how deposition varies continuously (Supplementary Fig. 3), effectively interpolating between the model output of the simulations. We account for the influence of internal variability by adding a noise variance term to the deposition anomaly during the construction of the emulators such that we do not need to run conventional meteorological ensemble members for each eruption realisation (see Methods).

The combinations of eruption source parameters that lead to deposition within a measured range can be found by constraining the emulator predictions for all possible eruptions in our three-dimensional space (see Methods). To illustrate the constraint procedure we take the emulated deposition and find the source parameters of eruptions that lead to the ice-sheet sulfate deposition derived from ice cores[4] for the 1815 eruption of Mt. Tambora (Table 1). The three-dimensional constrained parameter spaces for each eruption season (i.e. the eruptions that lead to sulfate deposition of 39.7±10.4 kg km^{-2} in Greenland and 45.8±5.3 kg km^{-2} in Antarctica) are shown in Fig. 2. The uncertainties on the emulator predictions (that the emulator itself derives) are accounted for during the constraint: a combination of parameters (i.e. an eruption-realisation) is retained if the interval of the emulator mean prediction plus or minus one standard deviation (SD) overlaps with the uncertainty range of the ice-core-derived sulfate deposition estimate for both ice sheets.

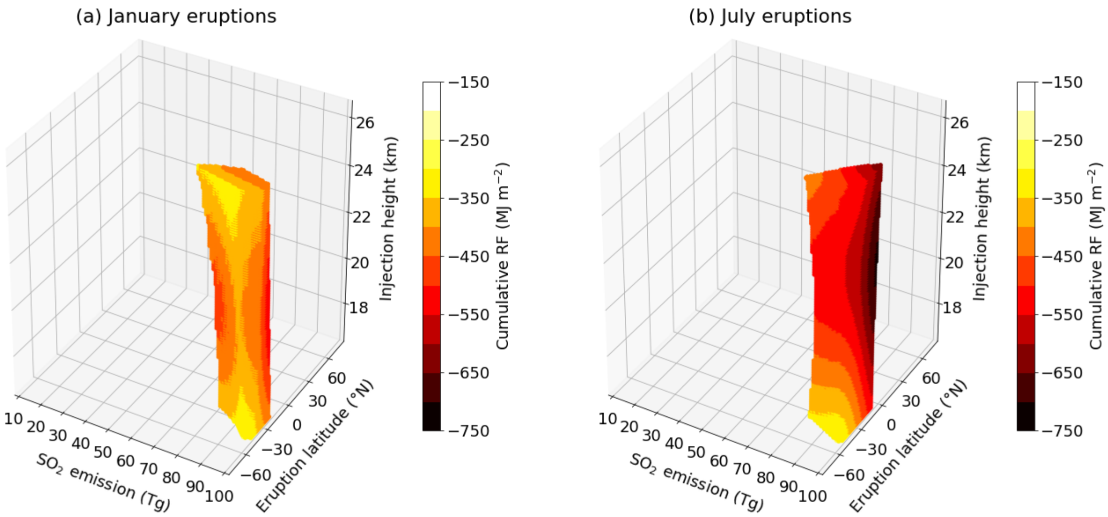

Fig. 2 Constrained parameter space showing the combinations of SO_2 emission, eruption latitude and injection height that result in the possible range of ice-core-derived sulfate deposition following 1815 Mt. Tambora[4] for January (a) and July (b) eruptions. Parameter combinations are retained if the emulator mean prediction plus or minus 1 SD for both the Antarctica and Greenland deposition overlaps with the ice-core-derived ranges (Table 1). The constrained space is made up of scatter points of the parameter combinations and the colour of each scatter point shows the corresponding emulator mean prediction of the time-integrated radiative forcing representing the potential climatic impact (cumulative radiative forcing (RF); Methods) for each of these eruptions. Injection height marks the middle of the 3-km-deep plume.

For an eruption occurring in January, the predicted deposition falls within both the Greenland and Antarctica deposition uncertainty ranges only if the SO_2 emission is greater than 73 Tg and the latitude of the eruption is between 20°S and 49°S. The injection height remains unconstrained. For an eruption in July, only eruptions with SO_2 emissions greater than 81 Tg and with a latitude between 4°S and 59°S can produce deposition that matches both ice sheet constraints. To match the ice sheet deposition for an eruption occurring at the latitude of Mt. Tambora (8°S), the eruption must occur in July and the SO_2 emission must be greater than 96 Tg. This emission is higher than the 60 Tg estimate often used to simulate this eruption in climate models[40,41], but closer to petrological estimates (73-91 Tg)[15]. We have built emulators only for eruptions occurring on 1 January and 1 July, whereas Mt. Tambora erupted in April 1815. The predicted deposition is generally higher in Greenland for January eruptions, and higher in Antarctica for July eruptions (Supplementary Fig. 3) and deposition following an April eruption would also differ given seasonally varying stratospheric transport of sulfate aerosol and depositional processes[17]. Furthermore, previous simulations of the 1815 eruption of Mt. Tambora using UM-UKCA with 60 Tg SO_2 emitted at the equator showed that sulfate deposited on the ice sheets was roughly half that derived from ice-core estimates[40]. This indicates that either the SO_2 emission used in the model was too low or that a structural error exists within the model resulting in a low bias in deposition. Background (non-volcanic) sulfate deposition simulated in UM-UKCA was found to compare well to ice-core estimates.

Constraining volcanic radiative forcing for the ten largest bipolar deposition signals

We now examine the full range of eruptions that could lead to the ice-core-derived deposition signals for the ten largest bipolar events in the last 2500 years[4]. Only two of these events have been confidently attributed to known eruptions (1815 Mt. Tambora, which is the 6th largest deposition signal, and 1257 Samalas, which is the 2nd largest deposition signal)[18]. For each eruption-realisation retained in the constraint, we examine the cumulative sAOD and cumulative RF predicted by the respective emulators (see Methods) to estimate the range in volcanic forcing that is consistent with each deposition signal.

Figures 3 and 4 show histograms of the constrained cumulative sAOD and RF for the ten events. Based on our model, there are no plausible eruption source parameter combinations for the 426 BCE and 1257 Samalas deposition (detected ice sheet deposition for this eruption starts in 1258 CE), and very few combinations for the 1458 CE deposition. This suggests that the SO_2 emissions of these eruptions exceed the 100 Tg bound of our parameter space, consistent with previous estimates[15,18,21,42]. Importantly, for the remaining deposition signals, many eruption realisations are retained with many different combinations of SO_2 emission, eruption latitude and injection height (Table 1, Supplementary Figs. 4-5), which lead to a large range in cumulative sAOD and RF for both January and July eruptions (Figs. 3 and 4).

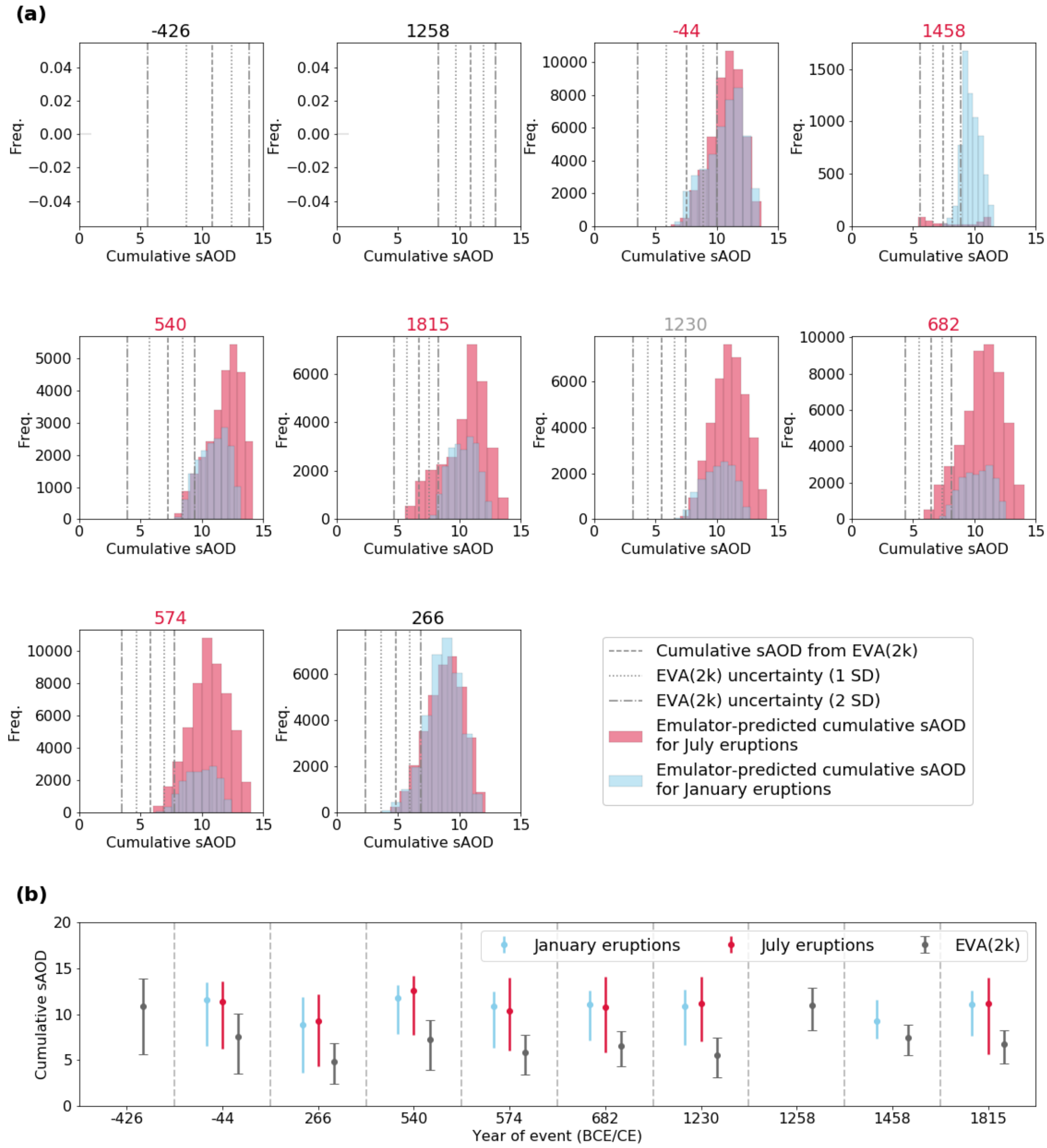

Fig. 3 (a) Range and distributions of the emulator-predicted cumulative sAOD (emulator mean) of retained eruption source parameter combinations for the ten largest bipolar deposition signals in the last 2500 years (in rank order of magnitude). The red distribution is the cumulative sAOD for July eruptions and the blue distribution is for January eruptions. Each histogram is plotted using 10 bins. The vertical grey dashed lines mark the cumulative sAOD derived for each of these eruptions from the PMIP4 EVA(2k) dataset using upper and lower estimates (1 SD and 2 SD) of the stratospheric

SO_2 emissions (see Methods). The year (BCE/CE) of the onset of each deposition signal is shown at the top of each panel and colour-coded depending on whether the constrained space is capped at 100 Tg. The title is grey if only the July eruptions are capped at 100 Tg, red if both January and July eruptions are capped at 100 Tg and black if neither of the sets of eruptions are capped at 100 Tg. **(b)** Range in the cumulative sAOD for all events from the two emulators (red and blue lines) and from EVA(2k) (grey lines). The circles mark the modal sAOD value of each of the constrained distributions and the sAOD value from EVA(2k) using the median estimate of the stratospheric SO_2 emission (see Methods). The error bars remain uncapped for the emulator-predictions because these uncertainties will be larger given the 100 Tg bound of our parameter space and the emulator uncertainties. Because so few combinations of parameters are retained for July eruptions matching the 1458 deposition signals, this data is not shown in panel (b).

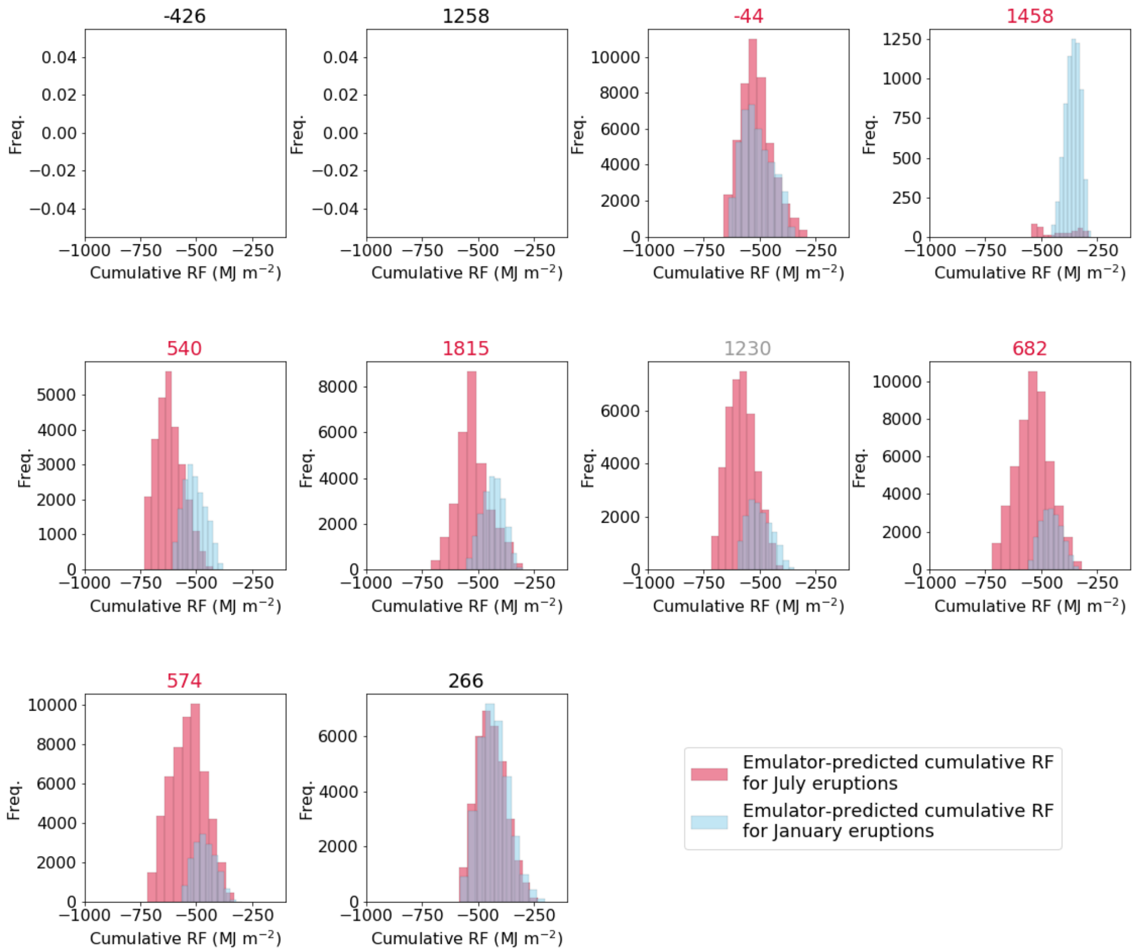

Fig. 4 Range and distributions of the emulator-predicted cumulative RF (emulator mean) of retained eruption source parameter combinations for the ten largest bipolar deposition signals in the last 2500 years (in rank order of magnitude). The red distribution is the cumulative RF for July eruptions and the blue distribution is for January eruptions. Each histogram is plotted using 10 bins. The year (BCE/CE) of the onset of each deposition signal is shown at the top of each panel and colour-coded depending on whether the constrained space is capped at 100 Tg. The title is grey if only the July eruptions are capped at 100 Tg, red if both January and July eruptions are capped at 100 Tg and black if neither of the sets of eruptions are capped at 100 Tg.

The largest range in cumulative sAOD constrained for a single season is 8.4 (summed over 38 months) for a July 1815 Mt. Tambora eruption. Although we know the latitude of Mt. Tambora, we retain the whole range in the constrained set of parameter combinations as an example of if the eruption had not been attributed. This range in sAOD translates into a cumulative RF between -300 and -710 MJ m^{-2} (i.e. a range of 410 MJ m^{-2}). The largest range in cumulative sAOD across the minimum and maximum constrained values from both seasons is 8.5 for the 266 CE deposition. However, the largest range across both seasons in cumulative RF occurs for the 574 CE deposition (424 MJ m^{-2}). This largest sAOD does not correspond to the largest RF because the RF is also dependent on the insolation, surface albedo and cloud cover. This difference further highlights the potential error associated with using a fixed factor to convert global mean sAOD to RF in previous reconstructions. The smallest range across both seasons in cumulative sAOD is 6.1 and in cumulative RF is -267 MJ m^{-2}, both for the 1458 CE deposition. However, this small range only occurs because the eruption-realisations were capped at 100 Tg of SO_2.

The constrained cumulative RF values are different for eruptions in different seasons (Fig. 4) because different combinations of parameters are retained and because, for the same combinations of parameters, cumulative RF can differ between seasons. Emulator-predicted cumulative RF for eruptions across the three-dimensional parameter space and in both seasons are shown in Fig. 5. The highest cumulative RF occurs for eruptions at the equator if they occur in July, but for tropical eruptions south of the equator if they occur in January (Fig. 5), likely because of seasonal variations in the position and strength of the tropical pipe that controls hemispheric transport[43,44]. Mid-latitude eruptions also lead to stronger cumulative RF if they occur in winter because it takes up to 8 months for the peak aerosol burden to be reached (in the UM-UKCA simulations) and the highest aerosol burden subsequently coincides with peak summer insolation.

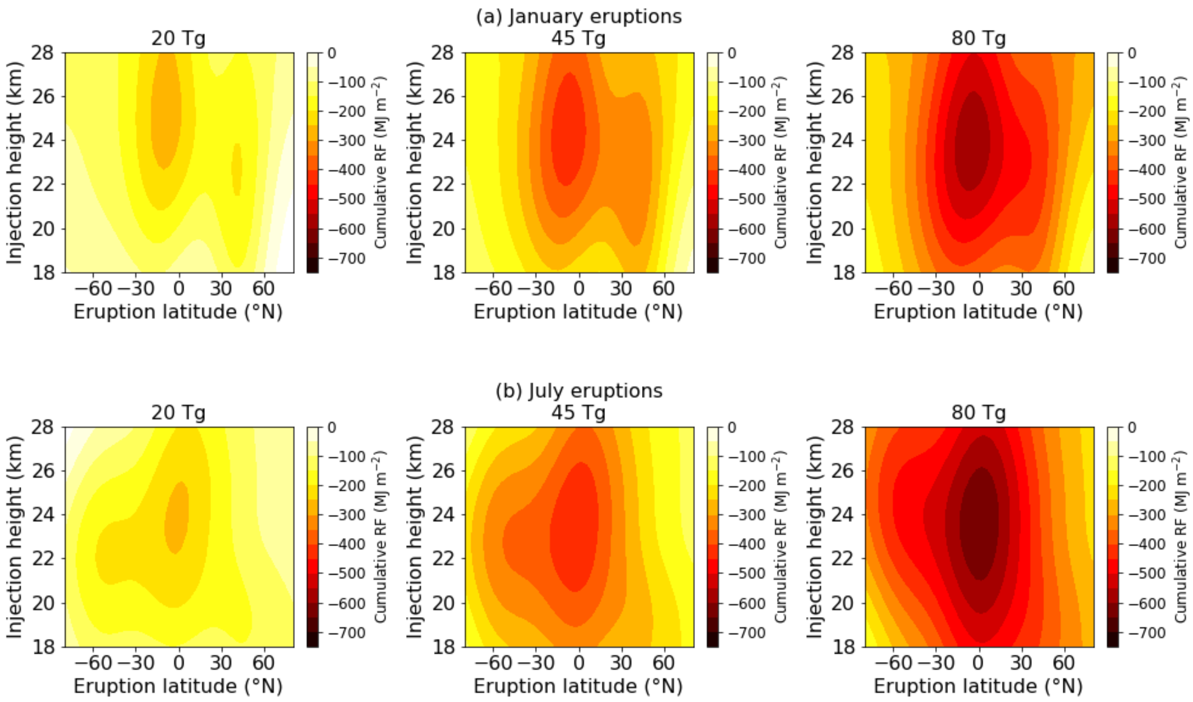

Fig. 5 Emulated response surfaces of the cumulative RF at fixed SO_2 emissions of 20 Tg, 45 Tg and 80 Tg for January eruptions (a) and July eruptions (b) (as in Figure 7 in Marshall et al. (2019)[37]). The contour plots show the emulator mean prediction of cumulative RF against the latitude and injection height of the emissions for each of these emission magnitudes. The injection height values are the middle of the 3-km plume.

Except for the 44 BCE and 266 CE deposition, the cumulative RF of the retained July eruptions reach larger values (more negative) compared to the retained January eruptions and more combinations are retained in total for the July eruptions (except 1458). Compared to the January retained eruptions, the July retained eruptions are either shifted towards the NH or expanded further into both hemispheres, reaching stronger values of cumulative RF near the equator (Supplementary Figs. 4-5). Tropical NH eruptions occurring in January would lead to higher Greenland deposition and lower Antarctic deposition because more aerosol is transported to the NH and deposition would fall outside of the ice sheet constraints. Several of the retained January eruptions also have combinations with lower SO_2 emissions than the July combinations.

The 44 BCE and 266 CE eruptions deposit much more sulfate on Greenland than on Antarctica (a ratio of 6.5 and 5.4, respectively) than the other eruptions (ratios are less than 2.4). Consequently, the January retained eruptions are in the tropics and the July retained eruptions are shifted towards the NH mid-latitudes (especially for 44 BCE) with the closer proximity of these eruptions to Greenland balancing the reduction in poleward transport due to being in the summer hemisphere. The range in retained SO_2 emissions is also similar between seasons for both cases and therefore the similar cumulative RF distributions despite differences in eruption latitude may be because of differences in cumulative RF related to the position and strength of the tropical pipe (Fig. 5).

For all ten events, the injection height across all retained parameter combinations is not constrained, although there are some combinations of SO_2 emission and eruption latitude where injection height is slightly constrained. Supplementary Fig. 4 shows that the January constrained parameter space is often sloped, with lower emissions that have the highest injection heights, and higher emissions with lower injection heights. The lack of constraint is important since although the time-integrated deposition is generally not sensitive to the injection height, the cumulative RF is (Fig. 5). The injection height is likely more important for the timing of the ice sheet deposition.

Our estimated mean values of plausible SO_2 emissions for each eruption are generally higher than the volcanic stratospheric sulfur injection (VSSI) estimates used to derive the PMIP4 prescribed sAOD timeseries, EVA(2k)[18] (Table 1), although our lower estimates overlap the upper VSSI estimates (except for the 1458 CE deposition). For the 540 CE eruption, our constrained parameters include the eruption latitude suggested by Toohey et al. (2016)[23] (15ºN) only if the eruption occurred in July, but do not include the emission (50 Tg). The equivalent cumulative sAOD for each of the 10 events from the EVA(2k) reconstruction are included in Fig. 3. Since our constrained SO_2 emissions reach higher values than the VSSI estimates, it is not surprising that the cumulative sAOD from EVA(2k) for each of the ten eruptions is towards the lower end, or in the case of the 1230 CE eruption, almost outside of our sAOD ranges. Our results consequently suggest that the EVA(2k) sAOD may be an underestimate. Our uncertainty ranges are also generally higher (Fig 3b).

Because the natural meteorological variability (accounted for as a noise variance term on the emulators) can cause further uncertainty on the predictions and can increase the probability that parameter combinations are retained (for example at higher latitudes), constrained parameter combinations obtained using only the emulator mean prediction of the deposition are also shown in the supplementary information (Supplementary Figs 6-9, Supplementary Table 1). Fewer plausible eruptions are retained for each of the ten events, but the overall uncertainty on cumulative sAOD and cumulative RF remains similar.

Table 1 Constrained ranges in SO_2 emission (Tg SO_2), eruption latitude (°N) and cumulative RF (MJ m^{-2}) for the ten largest bipolar ice-core-derived sulfate deposition signals in Greenland and Antarctica[4] (in rank order of magnitude). Year (BCE/CE) is the onset of the deposition signal. Also included are the eVolv2k[18] Volcanic Stratospheric Sulfur Injections (VSSI) (plus or minus 2 standard deviations) (Tg of SO_2). For all cases the minimum and maximum retained injection plumes were 15-18 km and 25-28 km. Grey shading marks signals that are unconstrained because they are outside of our parameter space. Although the latitude of 1815 Mt. Tambora is known, we keep the whole range in constrained parameters as an example for if the eruption had not been attributed. Values have been rounded to the nearest integer.

	Ice sheet deposition (kg SO_4 km^{-2})		**January eruptions**						**July eruptions**						
Year (BCE/CE)	**Greenland**	**Antarctica**	**Lat min**	**Lat max**	**SO_2 min**	**SO_2 max**	**RF min**	**RF max**	**Lat min**	**Lat max**	**SO_2 min**	**SO_2 max**	**RF min**	**RF max**	**VSSI**
-426	100±26	78±21													119±72
1258	90±24	73±9													119±43
-44	101±26	15±4	-9	44	55	100	-342	-638	7	80	62	100	-286	-660	77±45
1458	39±10	64±7	-65	-36	88	100	-276	-452	-61	-49	98	100	-286	-543	66±19
540	61±16	34±4	-28	-11	69	100	-381	-607	-27	17	75	100	-424	-730	64±31
1815	40±10	46±5	-49	-20	73	100	-300	-550	-59	-4	81	100	-300	-710	56±18
1230	56±15	23±3	-20	-4	50	99	-344	-598	-17	20	53	100	-394	-716	48±21
682	38±10	39±5	-40	-17	63	100	-331	-558	-51	-1	70	100	-319	-718	54±19
574	38±10	34±4	-35	-14	52	100	-294	-563	-44	1	62	100	-328	-717	48±20
266	61±16	11±1	-9	17	35	86	-198	-581	2	36	39	90	-230	-584	44±23

Discussion

We have constrained the eruption source parameters and the cumulative sAOD and cumulative RF of eruptions corresponding to the ten largest bipolar ice-sheet sulfate deposition fluxes over the past 2500 years, without relying on transfer functions and scaling factors derived from single eruptions. Our results suggest that there are many eruption realisations that could be consistent with ice-core-derived sulfate deposition fluxes, thus estimates of volcanic radiative forcing are more uncertain than previously thought.

The cumulative RF has an uncertainty of at least ~300 MJ m^{-2} for the ten historical eruptions over the last 2500 years that we have analysed, and can be as high as 424 MJ m^{-2}. To put this uncertainty range in context, the cumulative RF predicted for the 1991 eruption of Mt. Pinatubo has been estimated to be between -133 and -229 MJ m^{-2} [37] and is -203 MJ m^{-2} in the IPCC AR5[1] volcanic forcing series (integrated over 1991 to 1996). Our *uncertainty range* on the cumulative RF of these ten past eruptions therefore equates to approximately 1.5 to 3 times the total RF of 1991 Mt. Pinatubo. The 1991 eruption of Mt. Pinatubo led to up to 0.5°C of global surface cooling[45], so we estimate that the global mean temperature response to past eruptions could be uncertain to within at least 1.5°C, assuming that temperatures respond linearly to forcing[1]. The eruptions have a range in cumulative RF because there are many combinations of eruption latitude, SO_2 emission, emission height and season that produce ice-sheet sulfate deposition values that are consistent with measured anomalies. These variations in eruption source parameters affect the amount of aerosol that is formed, the particle size distribution, the horizontal and vertical distribution of the aerosol, its lifetime and hence its radiative effect[37].

Our constrained SO_2 emissions are at the higher end of previous estimates (eVolv2k[18]) used to derive the EVA(2K) PMIP4 forcing reconstruction, suggesting that the transfer functions used to link ice sheet deposition fluxes and stratospheric sulfate burdens do not hold for eruptions larger than 1991 Mt. Pinatubo (in agreement with Toohey et al. (2013)[22]). Alternatively, there may be a structural bias in UM-UKCA that leads to too-low polar ice-sheet deposition. Even if the latter is true, a large range in the volcanic forcing for each deposition event would still be retained given a range of eruption source parameter combinations, regardless of the absolute magnitude. Extension of our approach to other climate models would answer this question.

A large range in volcanic forcing for past eruptions has important implications for understanding and attributing climate variability on millennial timescales because different volcanic forcings will lead to different climate responses. Only one realisation of EVA(2k) with the medium VSSI predictions will be used in PMIP4, thus none of this uncertainty will be accounted for. Our results also suggest there are many other latitudes other than 0°N (to which unidentified eruptions leading to bipolar deposition signals are assigned) that could lead to the deposition signals, and more often than not these are south of the equator, especially if the eruption occurred in January. Hence, the assumption that eruptions occurred at 0°N may not be realistic.

Our estimated radiative forcing uncertainty ranges are likely to be lower bounds for several reasons. Our SO_2 emissions were capped at 100 Tg; we considered eruptions only in January and July and during the easterly QBO phase; we considered only one standard deviation uncertainty on the emulator-predicted deposition and on the ice-core-derived ice sheet estimates during constraint; and we did not include the emulator uncertainty on the sAOD and RF predictions, which was found during validation to be very small (see Methods).

The difficulty in quantifying volcanic deposition anomalies in the model simulations and the uncertainty in the emulator predictions are limitations of this study. It is possible that some of the retained parameter combinations, especially at high latitudes, could be false positives that arise due to variations in the non-volcanic sulfate deposition or due to the uncertainty in the emulator predictions. However, this is also applicable to the real world. Our results have revealed that many eruptions could be missed in the ice core records, or the volcanic sulfate deposition could be overestimated because of internal variability and false attribution.

This study is a step forward in estimating some of the uncertainty inherent in calculating the radiative forcing of past eruptions. Instead of using just one realisation of the potential volcanic aerosol forcing, this uncertainty should be accounted for in model simulations to facilitate a more complete and robust understanding of millennial climate change.

Methods

Model simulations

Simulations of volcanic eruptions were performed with the UM-UKCA state-of-the-art interactive stratospheric aerosol microphysics model (UK Hadley Centre Unified Model HadGEM3 coupled with version 8.4 of the UK Chemistry and Aerosol scheme) as outlined in Marshall et al. (2019)[37]. The model has a horizontal resolution of 1.875° longitude by 1.25° latitude with 85 vertical levels up to 85 km and has an internally generated Quasi Biennial Oscillation (QBO)[46]. The simulations were atmosphere-only and free running, with year 2000 background conditions that included prescribed climatological sea surface temperatures and sea ice extent[47].

Aerosol processes were simulated using the GLOMAP-mode aerosol microphysics scheme[48], with aerosol mass and number concentrations simulated using seven log-normal modes. GLOMAP-mode includes primary emissions, new particle formation, condensation, coagulation, cloud processing, sedimentation and dry and wet deposition. In the version used here, UM-UKCA includes stratospheric and tropospheric chemistry[49,50] and aerosols, interactive sulfur chemistry, and aerosol radiative heating, which has been shown to influence volcanic plume dispersion and subsequent radiative effects[51,52].

Two ensembles of simulations were conducted, each containing 41 eruptions with different values of three eruption source parameters: the mass of SO_2 emitted, the eruption latitude and the emission injection height[37]. SO_2 emissions ranged between 10 and 100 Tg of SO_2, eruption latitude ranged between 80°S and 80°N, and the bottom injection height varied between 15 and 25 km with a plume depth of 3 km (i.e. injections from 15-18 km to 25-28 km). One ensemble was performed for eruptions on 1 January and the other for eruptions on 1 July to examine the seasonal dependence of meridional stratospheric aerosol transport and sulfate deposition. The values of the eruption source parameters for each ensemble simulation were selected by using a ‘maximin’ Latin hypercube design (Supplementary Fig. 10) to achieve good coverage of the three-dimensional parameter space [53,54]. Each eruption (simulation) was initialized by injecting the SO_2 into the grid boxes within the 3-km plume over 24 hours on the first day of the month. Both ensembles were initialized during similar easterly QBO phases. Two control simulations were also conducted without any volcanic perturbation, initialized from the same point as each ensemble. The two control simulations together provided 9 years of background data. The ensemble simulations were run for 38 months post eruption (defined by the amount of computational resource available), by which time the majority (at least 83%, mean = 93%) of the injected sulfur had been deposited as sulfate.

The simulated sulfate deposited in each month (kg SO_4 km^{-2}) was calculated by summing the dry and wet deposition flux components (kg SO_4 km^{-2} s^{-1}) for each aerosol mode and multiplying by the number of seconds in each month (our simulations are run using 30-day months). The volcanic sulfate deposition was determined by subtracting the climatological monthly mean sulfate deposition derived from the 9 years of control simulation. These anomalies were integrated over the 38 months (~3 years) of each simulation to produce the total volcanic sulfate deposition. Time-integrated effective radiative forcing was similarly calculated by summing the net (shortwave + longwave) top-of-the-atmosphere outgoing all-sky global-mean radiative flux anomalies over the 38 months of the simulation. This metric consequently represents the cumulative impact of each eruption. Radiative flux anomalies were derived from a control simulation initialized at the same point as the volcanic simulations. We use the term ‘cumulative RF’ to refer to the time-integrated global mean effective radiative forcing (in MJ m^{-2}). Additionally, we also examine the time-integrated (summed over 38 months) volcanic anomalies in global mean stratospheric aerosol optical depth (sAOD) at 550 nm, which we refer to as ‘cumulative sAOD'. sAOD is dimensionless, so time-integrated sAOD has units of time (months), however for readability these units are omitted from the text.

Statistical emulation

Statistical emulators are used as surrogate statistical representations of the UM-UKCA model output, which can be evaluated in a fraction of the time (seconds) compared to the simulations themselves (weeks). An emulator maps a model output (e.g. total sulfate deposited on Greenland) to the input parameters (here the SO_2 emission, eruption latitude and injection height) and can be used to predict that model output for any combination of the input parameters that was not explicitly simulated. By sampling from an emulator thousands of times, a multi-dimensional response surface of the model output can be generated across the input parameter space, based on only a small set of model simulations.

We generated four Gaussian process emulators [54-56] of the simulated deposition: total sulfate deposited on Greenland following eruptions in January and July, and total sulfate deposited on Antarctica following eruptions in January and July. Each emulator was constructed using R[57] and the DiceKriging package[58]. Following a Bayesian statistical approach, each model response is assumed a priori to follow a Gaussian process, which is then updated with the information in the model data from 30 of the 41 ensemble members, known as 'training runs', to generate a posterior Gaussian process that forms our emulator. The emulators are built assuming a linear mean function that includes all parameters and a Matérn covariance structure[59]. The emulator provides a mean prediction of the model output at any parameter combination in the parameter space along with an estimate of the variance in this prediction. These uncertainties increase with distance (in parameter space) from the training runs because there is less information on how the model output varies as a function of the input parameters. The remaining 11 simulations of each ensemble are used to validate the emulators by comparing the emulator mean prediction with uncertainty for the parameter combinations of each simulation to the actual model output of each simulation[60].

The amount of sulfate deposited on the ice sheets for a given atmospheric/stratospheric burden is a result of a chain of several processes that includes the large-scale stratospheric transport of sulfate aerosol, stratosphere-troposphere exchange and deposition. These processes, especially the deposition, are variable due to stratospheric variability (e.g. because of the QBO) and tropospheric meteorological variability such that varying the initial conditions of our free-running simulations could lead to different ice sheet sulfate deposition fluxes. Here, we do not run a meteorological ensemble for each training point in parameter space and cannot account for this internal variability in the conventional way. Instead, we account for the internal variability using an alternative method by adding a noise variance term when building the emulators[58]. The addition of this variance term allows the emulator to vary more smoothly such that the mean emulator prediction does not have to exactly pass through the model training data[61-64]. In this way, we can effectively characterize conventional ensemble member variability in the construction of the emulator with the emulator mean prediction reflecting a meteorological ensemble mean. The uncertainty on the emulator predictions accounts for the inherent emulator uncertainty and the additional noise term because of internal variability. This method negates the need for running conventional meteorological ensemble members and therefore reduces the computational cost of our experiment.

We include the additional variance due to internal variability by specifying an estimated variance on the model output of each training run during construction of the emulator. We choose to add a homogeneous noise term to each emulator and we estimate that the calculated sulfate deposition output has a standard deviation due to the internal variability of 10 kg SO_4 km^{-2} in Greenland and 2.5 kg SO_4 km^{-2} in Antarctica. These values were chosen based on prior knowledge of deposition in Antarctica and Greenland from previous modelling studies, from the deposition variability in previous UM-UKCA simulations, and whether the validation of the new emulator was improved compared to an emulator built without a noise term. For example, relative standard deviations (RSD) of 16% in Greenland and 9% in Antarctica due to the meteorological state have been suggested[18], based on ensembles of atmosphere-only simulations of eruptions with a range of SO_2 emission magnitudes from 8.5 to 700 Tg[22]. Similarly, another study[21] reported ~10-20% differences in sulfate deposition over Greenland and Antarctica amongst ensemble members following simulations of eruptions with SO_2 injections ranging from 5 to 122 Tg. We found that across 5 meteorological ensemble members of atmosphere-only simulations of UM-UKCA of the eruption of Mt. Tambora[40] (simulated during the easterly QBO phase), the standard deviation of the Greenland deposition was 6.2 kg SO_4 km^{-2} (RSD = 20%) and the standard deviation of Antarctica deposition was 1.6 kg SO_4 km^{-2} (RSD = 8%). Given that the simulation of Mt. Tambora was initialized with a 60 Tg SO_2 injection at the equator, it is reasonable that an average noise variance term for our ensemble with emissions spanning 10 to 100 Tg SO_2 and across both high and low latitudes, is higher. Regardless of the value of estimated noise, we found that the overall shape and pattern of the emulated surfaces remained the same but the emulator validation was improved using the given values. We found that higher estimates of this noise variance led to poorer emulator validation and response surfaces with reduced variation in model output versus the eruption source parameters. These values remain a best-estimate and reflect the average variability in deposition across the whole parameter space and across both seasons. Although it is possible to specify a heterogeneous noise term, it is likely this would introduce greater uncertainty given a lack of information as to how internal variability terms may vary across the parameter space. Because our simulations use prescribed SSTs, internal variability associated with ENSO is not included. Similarly, we do not investigate variability associated with different QBO phases.

We built four further Gaussian process emulators of the cumulative RF and cumulative sAOD for each season (for eruptions occurring in January and July). These emulators were built without noise because the sAOD and radiative forcing signals have relatively low variability compared to the deposition (they are not determined by tropospheric meteorology) and validation of the emulators was reasonable without an additional noise term.

Validation of the emulators is shown in Supplementary Figs. 11 and 12. The emulator predictions follow the 1:1 line (marking a perfect prediction by the emulator) in all cases. The 95% confidence bounds on the emulator predictions are larger for the deposition emulators (Supplementary Fig. 11) compared to the cumulative sAOD and RF emulators (Supplementary Fig. 12) because the fit is more uncertain and because of the additional noise term in the build. Overall, the emulators are reasonable surrogates of the UM-UKCA output. Emulated response surfaces of the model outputs were produced by sampling the predicted response of each emulator 1 million times over a three-dimensional grid generated with 100 values of each eruption source parameter (covering the range in values simulated for each parameter).

Constraining the eruption-realisations

Eruption-realisations are retained if the emulator-mean prediction of the Antarctica deposition plus or minus one standard deviation and the emulator-mean prediction of the Greenland deposition plus or minus one standard deviation overlaps with the ice-core-derived estimates and their uncertainty[4]. By including the emulator uncertainty on the deposition emulators (which also accounts for ensemble spread) and the uncertainty on the ice sheet composite observations, we provide a conservative estimate of the range in eruption source parameter combinations and subsequently the range in cumulative RF for the parameter space we have investigated. We repeat the constraint procedure using the emulator-mean predictions only (without using the emulator standard deviation, so only retaining combinations where the mean prediction lies within the observed range) to show the more constrained estimates of plausible parameter combinations (Supplementary Figs 6-9, Supplementary Table 1). Most (except 44 BCE and 266 CE) of the ten ice-sheet deposition constraints we consider are large enough in magnitude that it is unlikely that these signals could be produced by non-volcanic sulfate anomalies in our simulations (i.e. they are much greater than 20 kg SO_4 km^{-2} on Greenland and 10 kg SO_4 km^{-2} on Antarctica where a clearer volcanic signal is observed in our simulations (Fig. 1)).

We constrain preindustrial sulfate deposition signals from simulations conducted using a present-day atmosphere, where the background non-volcanic sulfate emissions are higher and large-scale atmospheric circulation is faster. However, we find that the emulators predict the deposition following the 1815 eruption of Mt. Tambora from preindustrial UM-UKCA simulations[40] and therefore this difference is unlikely to significantly impact our results.

The EVA(2k) sAOD reconstruction is calculated using the Easy Volcanic Aerosol (EVA) forcing generator [35] and Volcanic Stratospheric Sulfur Injections (VSSI) from the eVolv2k reconstruction[18]. The sAOD timeseries for each of the 10 eruptions from the EVA(2k) reconstruction are shown in Supplementary Fig. 13. We used five runs of EVA (with no background aerosol included) that were run using the lower-end, middle and upper-end VSSI SO_2 estimates and isolated our 10 eruptions (upper and lower injections were calculated by summing/subtracting the one and two standard deviation uncertainties from the middle best-estimate predictions). For each eruption we summed the sAOD over 38 months to compare directly to the cumulative sAOD derived from the UM-UKCA simulations. The resulting cumulative sAOD from the three runs are shown by the vertical lines in Fig. 3.

Data Availability

Model output is included in Supplementary Table 2.

References

1. Myhre, G. *et al.* in *Climate Change 2013: The Physical Science Basis. Contribution of Working Group I to the Fifth Assessment Report of the Intergovernmental Panel on Climate Change* (eds T.F. Stocker *et al.*) (Cambridge University Press, 2013).
2. Hegerl, G. C. *et al.* Detection of human influence on a new, validated 1500-year temperature reconstruction. *Journal of Climate* **20**, 650-666, doi:10.1175/jcli4011.1 (2007).
3. Crowley, T. *et al.* Volcanism and the little ice age. *PAGES Newsletter* **16**, 22-23 (2008).
4. Sigl, M. *et al.* Timing and climate forcing of volcanic eruptions for the past 2,500 years. *Nature* **523**, 543–549, doi:10.1038/nature14565 (2015).
5. Schmidt, G. A. *et al.* Climate forcing reconstructions for use in PMIP simulations of the last millennium (v1.0). *Geoscientific Model Development* **4**, 33-45, doi:10.5194/gmd-4-33-2011 (2011).
6. Jungclaus, J. H. *et al.* The PMIP4 contribution to CMIP6-Part 3: The last millennium, scientific objective, and experimental design for the PMIP4 past1000 simulations. *Geoscientific Model Development* **10**, 4005-4033, doi:10.5194/gmd-10-4005-2017 (2017).
7. Carn, S. A., Clarisse, L. & Prata, A. J. Multi-decadal satellite measurements of global volcanic degassing. *Journal of Volcanology and Geothermal Research* **311**, 99-134, doi:10.1016/j.jvolgeores.2016.01.002 (2016).
8. Sato, M., Hansen, J. E., McCormick, M. P. & Pollack, J. B. Stratospheric Aerosol Optical Depths, 1850-1990. *Journal of Geophysical Research-Atmospheres* **98**, 22987-22994, doi:10.1029/93jd02553 (1993).
9. Stothers, R. B. Major optical depth perturbations to the stratosphere from volcanic eruptions: Pyrheliometric period, 1881-1960. *Journal of Geophysical Research-Atmospheres* **101**, 3901-3920, doi:10.1029/95jd03237 (1996).
10. Stothers, R. B. Major optical depth perturbations to the stratosphere from volcanic eruptions: Stellar extinction period, 1961-1978. *Journal of Geophysical Research-Atmospheres* **106**, 2993-3003, doi:10.1029/2000jd900652 (2001).
11. Devine, J. D., Sigurdsson, H., Davis, A. N. & Self, S. Estimates of sulfur and chlorine yield to the atmosphere from volcanic eruptions and potential climatic effects. *Journal of Geophysical Research* **89**, 6309-6325, doi:10.1029/JB089iB07p06309 (1984).
12. Scaillet, B. J., Luhr, F. & Carroll, M. R. in *Volcanism and the Earth's Atmosphere* (eds A. Robock & C. Oppenheimer) 11–40 (AGU, 2003).
13. Self, S., Gertisser, R., Thordarson, T., Rampino, M. R. & Wolff, J. A. Magma volume, volatile emissions, and stratospheric aerosols from the 1815 eruption of Tambora. *Geophysical Research Letters* **31**, doi:10.1029/2004gl020925 (2004).
14. Metzner, D. *et al.* Radiative forcing and climate impact resulting from SO2 injections based on a 200,000-year record of Plinian eruptions along the Central American Volcanic Arc. *International Journal of Earth Sciences* **103**, 2063-2079, doi:10.1007/s00531-012-0814-z (2014).
15. Vidal, C. M. *et al.* The 1257 Samalas eruption (Lombok, Indonesia): the single greatest stratospheric gas release of the Common Era. *Scientific Reports* **6**, doi:10.1038/srep34868 (2016).
16. Sigl, M. *et al.* Insights from Antarctica on volcanic forcing during the Common Era. *Nature Climate Change* **4**, 693-697, doi:10.1038/nclimate2293 (2014).

17 Gao, C., Robock, A. & Ammann, C. Volcanic forcing of climate over the past 1500 years: An improved ice core-based index for climate models. *Journal of Geophysical Research-Atmospheres* **113**, doi:10.1029/2008jd010239 (2008).

18 Toohey, M. & Sigl, M. Volcanic stratospheric sulfur injections and aerosol optical depth from 500 BCE to 1900 CE. *Earth System Science Data* **9**, 809-831, doi:10.5194/essd-9-809-2017 (2017).

19 Crowley, T. & Unterman, M. B. Technical details concerning development of a 1200 yr proxy index for global volcanism. *Earth System Science Data* **5**, 187-197, doi:10.5194/essd-5-187-2013 (2013).

20 Clausen, H. B. & Hammer, C. U. The Laki and Tambora eruptions as revealed in Greenland ice cores from 11 locations. *Annals of Glaciology* **10**, 16-22 (1988).

21 Gao, C., Oman, L., Robock, A. & Stenchikov, G. L. Atmospheric volcanic loading derived from bipolar ice cores: Accounting for the spatial distribution of volcanic deposition. *Journal of Geophysical Research-Atmospheres* **112**, doi:10.1029/2006jd007461 (2007).

22 Toohey, M., Kruger, K. & Timmreck, C. Volcanic sulfate deposition to Greenland and Antarctica: A modeling sensitivity study. *Journal of Geophysical Research-Atmospheres* **118**, 4788-4800, doi:10.1002/jgrd.50428 (2013).

23 Toohey, M., Kruger, K., Sigl, M., Stordal, F. & Svensen, H. Climatic and societal impacts of a volcanic double event at the dawn of the Middle Ages. *Climatic Change* **136**, 401-412, doi:10.1007/s10584-016-1648-7 (2016).

24 Robock, A. & Free, M. P. Ice cores as an index of global volcanism from 1850 to the present. *Journal of Geophysical Research-Atmospheres* **100**, 11549-11567, doi:10.1029/95jd00825 (1995).

25 Pinto, J. P., Turco, R. P. & Toon, O. B. Self-limiting physical and chemical effects in volcanic eruption clouds. *Journal of Geophysical Research-Atmospheres* **94**, 11165-11174, doi:10.1029/JD094iD08p11165 (1989).

26 Timmreck, C. *et al.* Aerosol size confines climate response to volcanic super-eruptions. *Geophysical Research Letters* **37**, doi:10.1029/2010gl045464 (2010).

27 Stothers, R. B. The Great Tambora Eruption in 1815 and Its Aftermath. *Science* **224**, 1191-1198, doi:10.1126/science.224.4654.1191 (1984).

28 Hansen, J. *et al.* Efficacy of climate forcings. *Journal of Geophysical Research-Atmospheres* **110**, doi:10.1029/2005jd005776 (2005).

29 Lacis, A., Hansen, J. & Sato, M. Climate forcing by stratospheric aerosols. *Geophysical Research Letters* **19**, 1607-1610, doi:10.1029/92gl01620 (1992).

30 Andersson, S. M. *et al.* Significant radiative impact of volcanic aerosol in the lowermost stratosphere. *Nature Communications* **6**, doi:10.1038/ncomms8692 (2015).

31 Gregory, J. M., Andrews, T., Good, P., Mauritsen, T. & Forster, P. M. Small global-mean cooling due to volcanic radiative forcing. *Climate Dynamics* **47**, 3979-3991, doi:10.1007/s00382-016-3055-1 (2016).

32 Larson, E. J. L. & Portmann, R. W. A Temporal Kernel Method to Compute Effective Radiative Forcing in CMIP5 Transient Simulations. *Journal of Climate* **29**, 1497-1509, doi:10.1175/JCLI-D-15-0577.1 (2016).

33 Schmidt, A. *et al.* Volcanic Radiative Forcing From 1979 to 2015. *Journal of Geophysical Research: Atmospheres* **123**, 12,491-412,508, doi:10.1029/2018jd028776 (2018).

34 Wigley, T. M. L., Ammann, C. M., Santer, B. D. & Raper, S. C. B. Effect of climate sensitivity on the response to volcanic forcing. *Journal of Geophysical Research-Atmospheres* **110**, doi:10.1029/2004jd005557 (2005).

35 Toohey, M., Stevens, B., Schmidt, H. & Timmreck, C. Easy Volcanic Aerosol (EVA v1.0): an idealized forcing generator for climate simulations. *Geoscientific Model Development* **9**, 4049-4070, doi:10.5194/gmd-9-4049-2016 (2016).

36 Toohey, M., Kruger, K., Niemeier, U. & Timmreck, C. The influence of eruption season on the global aerosol evolution and radiative impact of tropical volcanic eruptions. *Atmospheric Chemistry and Physics* **11**, 12351-12367, doi:10.5194/acp-11-12351-2011 (2011).

37 Marshall, L. *et al.* Exploring How Eruption Source Parameters Affect Volcanic Radiative Forcing Using Statistical Emulation. *Journal of Geophysical Research: Atmospheres* **0**, doi:10.1029/2018JD028675 (2019).

38 Toohey, M., Kruger, K., Bittner, M., Timmreck, C. & Schmidt, H. The impact of volcanic aerosol on the Northern Hemisphere stratospheric polar vortex: mechanisms and sensitivity to forcing structure. *Atmospheric Chemistry and Physics* **14**, 13063-13079, doi:10.5194/acp-14-13063-2014 (2014).

39 Kravitz, B. & Robock, A. Climate effects of high-latitude volcanic eruptions: Role of the time of year. *Journal of Geophysical Research-Atmospheres* **116**, doi:10.1029/2010jd014448 (2011).

40 Marshall, L. *et al.* Multi-model comparison of the volcanic sulfate deposition from the 1815 eruption of Mt. Tambora. *Atmospheric Chemistry and Physics* **18**, 2307-2328, doi:10.5194/acp-18-2307-2018 (2018).

41 Zanchettin, D. *et al.* The Model Intercomparison Project on the climatic response to Volcanic forcing (VolMIP): experimental design and forcing input data for CMIP6. *Geoscientific Model Development* **9**, 2701-2719, doi:10.5194/gmd-9-2701-2016 (2016).

42 Oppenheimer, C. Ice core and palaeoclimatic evidence for the timing and nature of the great mid-13th century volcanic eruption. *International Journal of Climatology* **23**, 417-426, doi:10.1002/joc.891 (2003).

43 Holton, J. R. *et al.* Stratosphere-Troposphere Exchange. *Rev. Geophys.* **33**, 403-439, doi:10.1029/95rg02097 (1995).

44 Seviour, W. J. M., Butchart, N. & Hardiman, S. C. The Brewer-Dobson circulation inferred from ERA-Interim. *Q. J. R. Meteorol. Soc.* **138**, 878-888, doi:10.1002/qj.966 (2012).

45 Dutton, E. G. & Christy, J. R. Solar radiative forcing at selected locations and evidence for global lower tropospheric cooling following the eruptions of El Chichón and Pinatubo. *Geophysical Research Letters* **19**, 2313-2316, doi:10.1029/92gl02495 (1992).

46 Osprey, S. M., Gray, L. J., Hardiman, S. C., Butchart, N. & Hinton, T. J. Stratospheric Variability in Twentieth-Century CMIP5 Simulations of the Met Office Climate Model: High Top versus Low Top. *Journal of Climate* **26**, 1595-1606, doi:10.1175/jcli-d-12-00147.1 (2013).

47 Reynolds, R. W. *et al.* Daily high-resolution-blended analyses for sea surface temperature. *Journal of Climate* **20**, 5473-5496, doi:10.1175/2007jcli1824.1 (2007).

48 Mann, G. W. *et al.* Description and evaluation of GLOMAP-mode: a modal global aerosol microphysics model for the UKCA composition-climate model. *Geoscientific Model Development* **3**, 519-551, doi:10.5194/gmd-3-519-2010 (2010).

49 Morgenstern, O. *et al.* Evaluation of the new UKCA climate-composition model - Part 1: The stratosphere. *Geoscientific Model Development* **2**, 43-57, doi:10.5194/gmd-2-43-2009 (2009).

50 O'Connor, F. M. *et al.* Evaluation of the new UKCA climate-composition model - Part 2: The Troposphere. *Geoscientific Model Development* **7**, 41-91, doi:10.5194/gmd-7-41-2014 (2014).

51 Aquila, V., Oman, L. D., Stolarski, R. S., Colarco, P. R. & Newman, P. A. Dispersion of the volcanic sulfate cloud from a Mount Pinatubo-like eruption. *Journal of Geophysical Research-Atmospheres* **117**, doi:10.1029/2011jd016968 (2012).

52 Mann, G. W. *et al.* Evolving particle size is the key to improved volcanic forcings. *Past Global Changes Magazine* **23**, 52-53 (2015).

53 Morris, M. D. & Mitchell, T. J. Exploratory designs for computational experiments. *Journal of Statistical Planning and Inference* **43**, 381-402, doi:https://doi.org/10.1016/0378-3758(94)00035-T (1995).

54 Lee, L. A., Carslaw, K. S., Pringle, K. J., Mann, G. W. & Spracklen, D. V. Emulation of a complex global aerosol model to quantify sensitivity to uncertain parameters. *Atmospheric Chemistry and Physics* **11**, 12253-12273, doi:10.5194/acp-11-12253-2011 (2011).

55 O'Hagan, A. Bayesian analysis of computer code outputs: A tutorial. *Reliability Engineering & System Safety* **91**, 1290-1300, doi:10.1016/j.ress.2005.11.025 (2006).

56 Johnson, J. S. *et al.* Evaluating uncertainty in convective cloud microphysics using statistical emulation. *Journal of Advances in Modeling Earth Systems* **7**, 162-187, doi:10.1002/2014ms000383 (2015).

57 RCoreTeam. (Vienna, Austria, 2017).

58 Roustant, O., Ginsbourger, D. & Deville, Y. DiceKriging, DiceOptim: Two R Packages for the Analysis of Computer Experiments by Kriging-Based Metamodeling and Optimization. *Journal of Statistical Software* **51**, 1-55 (2012).

59 Rasmussen, C. E. & Williams, C. K. I. *Gaussian Processes for Machine Learning*. (MIT Press, 2006).

60 Bastos, L. S. & O'Hagan, A. Diagnostics for Gaussian Process Emulators. *Technometrics* **51**, 425-438, doi:10.1198/TECH.2009.08019 (2009).

61 Johnson, J. S., Gosling, J. P. & Kennedy, M. C. Gaussian process emulation for second-order Monte Carlo simulations. *Journal of Statistical Planning and Inference* **141**, 1838-1848, doi:10.1016/j.jspi.2010.11.034 (2011).

62 Andrianakis, I. & Challenor, P. G. The effect of the nugget on Gaussian process emulators of computer models. *Computational Statistics & Data Analysis* **56**, 4215-4228, doi:10.1016/j.csda.2012.04.020 (2012).

63 Williamson, D., Blaker, A. T., Hampton, C. & Salter, J. Identifying and removing structural biases in climate models with history matching. *Climate Dynamics* **45**, 1299-1324, doi:10.1007/s00382-014-2378-z (2015).

64 Salter, J. M. & Williamson, D. A comparison of statistical emulation methodologies for multi-wave calibration of environmental models. *Environmetrics* **27**, 507-523, doi:10.1002/env.2405 (2016).

Acknowledgements

LM was funded by the U.K. Natural Environment Research Council (NERC) through the Leeds-York NERC Doctoral Training Program (NE/L002574/1). LM also acknowledges funding from NERC RG94689 (VOL-CLIM). AS, KSC, and GWM received funding from NERC grant NE/N006038/1 (SMURPHS). JSJ and KSC acknowledge funding from NERC grant NE/J024252/1 (GASSP) KSC acknowledges funding from NERC grant NE/P013406/1 (A-CURE). JSJ and KSC were supported by the U.K. China Research and Innovation Partnership Fund through the Met Office Climate Science for Service Partnership (CSSP) China as part of the Newton Fund. GWM received funding from the National Centre for Atmospheric Science (NCAS), one of the NERC research centers via the ACSIS long-term science program on the Atlantic climate system. KSC is currently a Royal Society Wolfson Merit Award holder.

We thank Matthew Toohey for providing the EVA(2k) simulations.

This work used the ARCHER UK National Supercomputing Service (http://www.archer.ac.uk) and JASMIN super-data-cluster (doi:10.1109/BigData.2013.6691556), via the Centre for Environmental Data Analysis (CEDA).

Author contributions

LM, AS, JSJ and KSC designed the study. LM conducted the model simulations and analysis. JSJ and LL provided guidance with statistical emulation. LM wrote the paper with guidance and assistance from AS, JSJ and KSC. GWM and LL contributed to editing the paper.

Competing Interests: The authors declare no competing interests.